Investigation of Exterior Rotor Bearingless Motor Topologies for High-Quality Mixing Applications

T. Reichert
T. Nussbaumer
J. W. Kolar

Investigation of Exterior Rotor Bearingless Motor Topologies for High-Quality Mixing Applications

Thomas Reichert, *Student Member, IEEE*, Thomas Nussbaumer, *Member, IEEE*, and Johann W. Kolar, *Fellow, IEEE*

***Abstract*—The selection of a suitable topology is a crucial part of the design process of a machine. In particular, the slot/pole combination of a bearingless motor has a strong influence on the levitation and drive characteristics. In this paper, several feasible slot/pole combinations for a bearingless motor in exterior rotor construction are investigated, and the important characteristics of each possible topology are discussed in detail. In the end, a comparison between the presented topologies is undertaken, and the optimal motor topology is designed and implemented in a prototype setup.**

***Index Terms*—Bearingless motor, brushless motor, concentrated windings, high torque, permanent magnet.**

I. INTRODUCTION

THE bearingless motor with exterior rotor can be advantageously employed for numerous emerging applications requiring high-purity or shear-sensitive mixing. Cell-protective stirring in a bioreactor [1]–[6] can be named as one of the prominent examples which can only be achieved if both requirements are fulfilled to a high level. State-of-the-art mixing systems, making use of either a sealing or a magnetic coupling, suffer from disadvantages that impact the demanded high-quality performance. Not only is a sealing not absolutely leakage proof but it also generates particles and leads to pinchoff areas that can harm the cell cultures in the reactor. A magnetic coupling, on the other hand, requires an additional bearing inside the tank for stability reasons, resulting in wear and pinchoff areas as well [7].

Using a bearingless motor [8]–[13] for the agitator allows for a completely wear-free setup, as is shown in Fig. 1. The stator is placed inside a tank indentation from outside of the reactor. From there, it is connected to the motor control (power electronics and sensor system, not shown in Fig. 1). The only component placed into the reactor is the impeller, which consists of the encapsulated rotor and mixer blades. Both bearing forces and torque are transmitted from the stator to
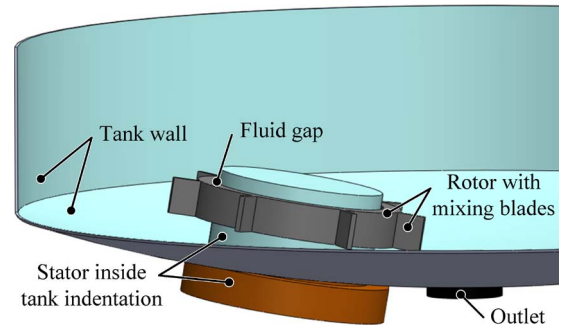
Fig. 1. Bearingless mixer implemented in a bioreactor. The stator is inside a tank indentation, and only the rotor (with the mixing blades) is put inside the tank. The rotor is levitated and absolutely free of contact to the reactor.

the rotor in a contactless manner. This means that, while the impeller is levitated, there is a sufficiently large fluid gap, which avoids the generation of pinchoff areas. Moreover, this fluid gap highly improves clean in place and sterilization in place [14]. Whenever the motor has to be powered down completely, the rotor is slowly moved toward the tank wall to a soft touchdown.

For the targeted mixing application, the motor has to deliver a high torque at moderate rotational speeds up to 500 r/min. For the bearing, sufficient forces (against radial, axial, and tilting disturbances) have to be generated in order to guarantee a minimum fluid gap over the whole angular range during the mixing process. The bearing combines passive forces, which stabilize the axial rotor position and counteract tilting, and active forces, which are required to stabilize the radial rotor position [15].

The promising capabilities of such a motor in mixing applications call for a detailed topology analysis. To date, there have been a few publications (e.g., [16], [17]) about specific topologies with exterior rotors. Additionally, the authors have published two articles [18], [19] about the design and setup of two specific topologies. However, a systematic evaluation which compares the different feasible bearingless motor topologies has not been presented in the literature so far. In this paper, different topologies for bearingless motors in exterior rotor construction are analyzed in terms of their torque and bearing force performance with the goal to clearly show the benefits and disadvantages of the different topologies. The control commands are derived in a general manner for four relevant stator topologies. Furthermore, important motor characteristics, i.e., cogging torque and unbalanced reluctance forces, are examined. In the end, a comparison of the feasible topologies is undertaken, and the most promising candidate is designed and implemented in a prototype setup.
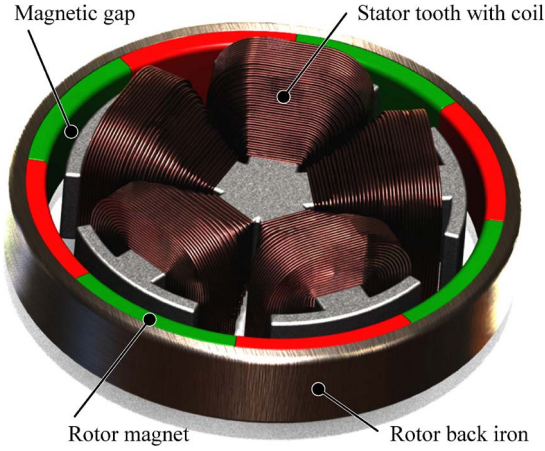
Fig. 2. Bearingless motor topology with five stator teeth and a rotor with pole pair number 4.

II. GENERAL FORCE AND TORQUE CALCULATION

Fig. 2 shows a possible topology of a bearingless motor in exterior rotor construction. The disk-shaped motor consists of a stator with a rotor ring placed around it, separated by the magnetic gap. The rotor can be distributed into permanent magnets and an iron ring being the back iron for the magnetic flux path. The permanent magnets are radially magnetized in alternating order. The stator consists of stator teeth with one concentrated coil [20] mounted on each of them. For the choice of a certain motor topology, the different combinations of rotor pole pair number p and stator slot number q have to be evaluated.

Prior to the analysis of specific topologies, a general force and torque calculation is carried out. In [21], the relation between the applied coil currents and the resulting bearing forces and torque has been formulated using the matrix $\mathbf{T}_m$

$$\begin{pmatrix} F_x \\ F_y \\ T \end{pmatrix} = \mathbf{T}_m \bullet \begin{pmatrix} i_1 \\ \vdots \\ i_q \end{pmatrix}. \tag{1}$$

$\mathbf{T}_m$ is a $3 \times q$ matrix, which depends on the current angular rotor position.

In practice, the control currents, for which a certain force or torque can be generated, have to be determined. Hence, the $\mathbf{T}_m$ matrix has to be inverted, leading to the $\mathbf{K}_m$ matrix. Since the $\mathbf{T}_m$ matrix is not necessarily quadratic, two calculation methods are proposed in [21] respecting different constraints. If the $\mathbf{K}_m$ matrix is calculated with

$$\mathbf{K}_m = \mathbf{T}_m^{\mathrm{T}} \bullet \left(\mathbf{T}_m \bullet \mathbf{T}_m^{\mathrm{T}} \right)^{-1} \tag{2}$$

the required coil currents become minimal. Alternatively, the calculation can be carried out under the constraint of a star connection of all phases. In this case

$$\mathbf{K}_m = \left(\mathbf{T}_m^{\mathrm{T}} - \frac{1}{q} \mathbf{1} \bullet \mathbf{1}^{\mathrm{T}} \bullet \mathbf{T}_m^{\mathrm{T}} \right)$$

$$\bullet \left(\mathbf{T}_m \bullet \left[\mathbf{T}_m^{\mathrm{T}} - \frac{1}{q} \mathbf{1} \bullet \mathbf{1}^{\mathrm{T}} \bullet \mathbf{T}_m^{\mathrm{T}} \right] \right)^{-1} \tag{3}$$

can be applied, where $\mathbf{1}$ represents a q times 1 vector filled with ones. If the summation of the entries in a row of the $\mathbf{T}_m$ matrix yields zero for each row, the calculation according to (3) can be reduced to (2).

Using the $\mathbf{K}_m$ matrix, the required currents to generate desired forces and torque can be calculated

$$\begin{pmatrix} i_1 \\ \vdots \\ i_q \end{pmatrix} = \mathbf{K}_m \bullet \begin{pmatrix} \tilde{F}_x \\ \tilde{F}_y \\ \tilde{T} \end{pmatrix}. \tag{4}$$

Ideally, a basic current shape such as that of sinusoidal currents is desirable because it is easier to implement in the control. For more complex current shapes, a detailed lookup table would be required.

As mentioned before, the $\mathbf{T}_m$ matrix depends on the angular rotor position, namely, the electrical angle φ_{elec}. A $360°$ revolution of this electrical angle corresponds with the angle of one rotor pole pair. Therefore, the relation between the mechanical rotor angle φ_{mech}, which describes a $360°$ revolution of the rotor, can be stated as

$$\varphi_{\mathrm{elec}} = p \cdot \varphi_{\mathrm{mech}}. \tag{5}$$

The force generation can be distributed into a tangential force (also referred to as Lorentz force) and a radial force (also referred to as Maxwell force), and they can both be analyzed for each stator tooth individually. In Fig. 3(a), the generation of a tangential force for one stator tooth (labeled 1) is shown. It reaches its maximum value for the angular position depicted with $\varphi_{\mathrm{elec}} = 90°$. It is assumed that the force has a sinusoidal dependence on this angular position. Then, introducing a tangential force–current factor $k_{I,\mathrm{Ft}}$, the tangential force becomes

$$F_{t,1}(\varphi_{\mathrm{elec}}) = k_{I,\mathrm{Ft}} \cdot \sin(\varphi_{\mathrm{elec}}) \cdot N_{\mathrm{coil}} \cdot I_1. \tag{6}$$

The force is proportional to the magnetomotive force, which is the product of the number of winding turns N_{coil} and the current through it (here, I_1). The comparison with the conventional calculation of the Lorentz force

$$F_{t,1}(\varphi_{\mathrm{elec}}) = \hat{B} \cdot \sin(\varphi_{\mathrm{elec}}) \cdot 2l \cdot N_{\mathrm{coil}} \cdot I_1 \tag{7}$$

reveals that the influence of the motor length and the amplitude of the magnetic flux density are expressed with the force–current factor $k_{I,\mathrm{Ft}}$.

Similarly, the radial force generated with one stator tooth reaches its maximum value for an angular rotor position which is $\varphi_{\mathrm{elec}} = 0°$ [see Fig. 3(b)]. A sinusoidal dependence on the rotor position is assumed as well, leading to a radial force of

$$\Delta F_{r,1}(\varphi_{\mathrm{elec}}) = k_{I,\mathrm{Fr}} \cdot \cos(\varphi_{\mathrm{elec}}) \cdot N_{\mathrm{coil}} \cdot I_1. \tag{8}$$

In this case, a radial force–current factor $k_{I,\mathrm{Fr}}$ has to be applied. Compared to the conventional calculation of the Maxwell force with

$$F_r(\varphi_{\mathrm{elec}}) = \frac{A \cdot B^2(\varphi_{\mathrm{elec}})}{2\mu_0} \tag{9}$$
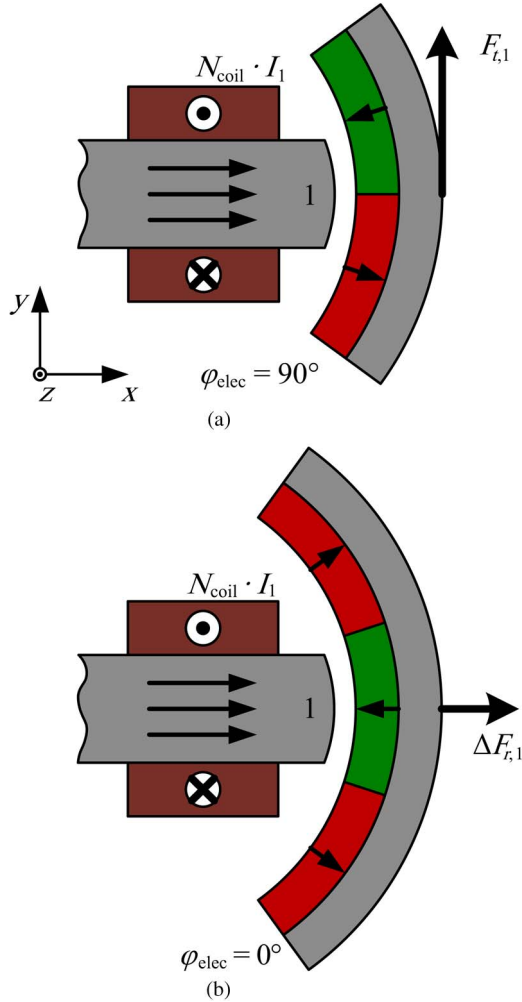
Fig. 3. Generation of a (a) tangential (Lorentz) and (b) radial (Maxwell) force in a bearingless motor.

the validity of (8) needs to be further elaborated. If no coil current is applied, the force generated between stator tooth 1 (Fig. 3) and the rotor depends on the flux density due to the permanent magnets

$$F_{r0,1}(\varphi_{\text{elec}}) = \frac{A \cdot B_{\text{PM},1}^2(\varphi_{\text{elec}})}{2\mu_0}. \tag{10}$$

In order to influence this force, a coil current can be applied which leads to a change in the magnetic flux density with order $\Delta B_1 (I_1)$. In this case, the radial force becomes

$$F_{r,1}(\varphi_{\text{elec}}) = \frac{A}{2\mu_0} \cdot [B_{\text{PM},1}(\varphi_{\text{elec}}) \pm \Delta B_1(I_1)]^2. \tag{11}$$

For small changes of the magnetic flux density, (11) can be simplified to

$$
\begin{aligned}
&F_{r,1}(\varphi_{\text{elec}}) \\
&= \frac{A}{2\mu_0} \cdot \left[B_{\text{PM},1}^2(\varphi_{\text{elec}}) \pm 2B_{\text{PM},1}(\varphi_{\text{elec}}) \cdot \Delta B_1(I_1) \right] \\
&= \underbrace{F_{r0,1}(\varphi_{\text{elec}})}_{(10)} \pm \underbrace{\frac{2A \cdot \hat{B}_{\text{PM},1} \cdot \cos(\varphi_{\text{elec}}) \cdot \Delta B_1(I_1)}{2\mu_0}}_{\to (8)}.
\end{aligned} \tag{12}
$$

Hence, the reluctance force consists of a part $F_{r0,1}$, which is the (angular dependent) reluctance force resulting from the permanent-magnet flux density. Based on the second part of (12), the application of (8) can be justified because ΔB is proportional to the coil current. If the proportionality factor and the remaining factors resulting in the second part of (12) are integrated into $k_{I,\text{Fr}}$, the linear relation is derived.

For many topologies, the net force (as the vector sum of all the radial forces produced with all the stator teeth) is zero when no coil current is applied because the Maxwell forces derived with (10) are equally balanced in each radial direction when the rotor is in its center position. However, there are certain topology configurations such as the five-slot motor (see further down) where an unbalanced magnetic pull takes effect on the rotor even at this inert position. In this case, the vector sum of all the individual reluctance forces $F_{r0,n}$ does not yield zero anymore. Nevertheless, if this unbalanced magnetic pull is simply treated like an offset F_{r0} (dependent on the angular rotor position, however), it can be subtracted first, which allows employing the previously derived radial force calculation in (8) for all topology variants. Any unbalanced reluctance force F_{r0} can simply be added to the total resulting force summed over all teeth (see further down) in the end.

For the torque generation, the situation is the same as for the generation of a tangential force. Introducing a torque–current factor $k_{I,\text{Tn}}$, the torque of one stator tooth becomes

$$T_1(\varphi_{\text{elec}}) = k_{I,\text{Tn}} \cdot \sin(\varphi_{\text{elec}}) \cdot N_{\text{coil}} \cdot I_1. \tag{13}$$

Up to now, only one stator tooth has been analyzed. Moreover, the stator tooth considered is aligned with the coordinate system. This means that the radial force corresponds with a force in the x-direction, whereas the tangential force corresponds with a force in the y-direction. If the analysis is expanded to all the stator teeth, the angular position of the stator teeth in relation to the fixed coordinate system has to be taken into account as well.

The net force into the x-direction can be derived as follows for any combination of p and q:

$$
\begin{aligned}
&F_x(\varphi_{\text{elec}}) \\
&= \sum_{n=1}^{q} \left[-\cos\left(\{n-1\} \cdot \frac{2\pi}{q} \right) \right. \\
&\qquad\qquad \cdot \cos\left((\varphi_{\text{elec}}) + \{n-1\} \cdot \frac{2\pi \cdot p}{q} \right) \\
&\qquad\qquad \cdot k_{I,\text{Fr}} + \sin\left(\{n-1\} \cdot \frac{2\pi}{q} \right) \\
&\qquad\qquad \left. \cdot \sin\left((\varphi_{\text{elec}}) + \{n-1\} \cdot \frac{2\pi \cdot p}{q} \right) \cdot k_{I,\text{Ft}} \right] \\
&\qquad\qquad \cdot N_{\text{coil}} \cdot I_{\text{bng},x,n}.
\end{aligned} \tag{14}
$$

For any combination of p and q, the force in y-direction becomes

$$F_y(\varphi_{\text{elec}})$$
$$= \sum_{n=1}^{q} \left[-\sin\left(\{n-1\} \cdot \frac{2\pi}{q}\right) \right.$$
$$\cdot \cos\left((\varphi_{\text{elec}}) + \{n-1\} \cdot \frac{2\pi \cdot p}{q}\right)$$
$$\cdot k_{I,\text{Fr}} + \cos\left(\{n-1\} \cdot \frac{2\pi}{q}\right)$$
$$\left. \cdot \sin\left((\varphi_{\text{elec}}) + \{n-1\} \cdot \frac{2\pi \cdot p}{q}\right) \cdot k_{I,\text{Ft}} \right]$$
$$\cdot N_{\text{coil}} \cdot I_{\text{bng},y,n}. \tag{15}$$

For the torque, there is no need to consider the geometrical relations of the stator teeth and the coordinate system because the tangential force always shows into the desired perpendicular direction. The torque can be derived as follows for any combination of p and q:

$$T(\varphi_{\text{elec}}) = \sum_{n=1}^{q} \sin\left((\varphi_{\text{elec}}) + \{n-1\} \cdot \frac{2\pi \cdot p}{q}\right) \cdot k_{I,\text{Tn}}]$$
$$\cdot N_{\text{coil}} \cdot I_{\text{drv},n}. \tag{16}$$

The force–current and torque–current factors are identical for each of the stator teeth. They can be derived through measurements or using a 3-D finite-element (FE) analysis.

For a q-slotted stator, q different possible setups have to be investigated, with the pole pair number varying from one to q ($p = 1, \ldots, q$). If the pole pair number is larger than the slot number, the control and the characteristics are identical to the corresponding case p^*, where $p^* < q$, using

$$p^* = p \mod q. \tag{17}$$

For the design (Section IV), topologies with a pole pair number larger than the slot number have to be considered too. However, their performance characteristics can always be derived from the case with a pole pair number below the slot number according to (17).

III. TOPOLOGY COMPARISON

The outer rotor diameter and the magnetic gap are usually defined by the targeted tank size. For this exterior rotor construction, the available space for the stator is very limited, as it has to be placed within the hollow rotor ring. Moreover, this scarce space has to be further divided into iron (stator teeth) and copper (windings) material. Therefore, it is recommendable to keep the number of stator teeth small because, otherwise, the iron would already cover up too much of the available area, leaving too little volume for the windings. Therefore, topologies with slot numbers from three to six will be investigated. Obviously, topologies with a higher slot number can also be realized
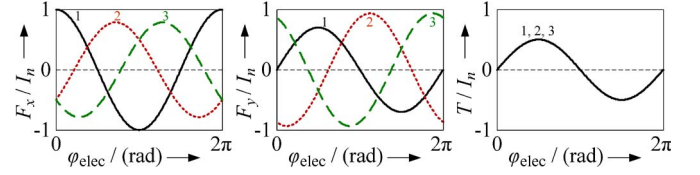

Fig. 4. $\mathbf{T}_m$ matrix of a bearingless motor with three stator teeth and a rotor with pole pair number 3. Here, and in the following, the three coil currents have been consolidated into one plot for the two bearing forces and the torque.
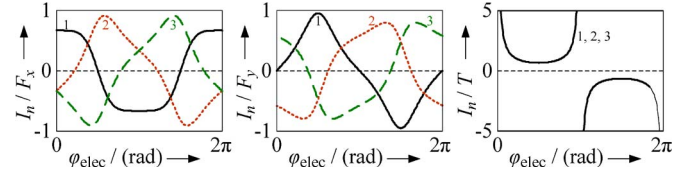

Fig. 5. $\mathbf{K}_m$ matrix of a bearingless motor with three stator teeth and a rotor with pole pair number 3. The torque currents converge to infinite, which means that the torque generation is zero for the corresponding angular rotor positions.

as bearingless mixers. However, they will not be examined in the scope of this paper for the aforementioned reason.

A. Motors With Three Stator Teeth

For motors with three stator teeth, the cases of $p = 1$, 2, and 3 have to be analyzed. For the first two cases, the $\mathbf{K}_m$ matrix can be calculated using direct matrix inversion, given that $\mathbf{T}_m$ is a 3×3 matrix for motors with three stator teeth. For example, the top left entry, which relates the current of coil 1 with a force into the x-direction becomes

$$\mathbf{K}_m(1,1) = \frac{4 \cdot k_{I,\text{Fr}} \cdot \sin(2 \cdot \varphi_{\text{elec}})}{3 \cdot \sin(3 \cdot \varphi_{\text{elec}}) \cdot \left(k_{I,\text{Fr}}^2 - k_{I,\text{Ft}}^2\right)} \tag{18}$$

for both cases with $p = 1$ or $p = 2$. This entry reveals that no bearingless motor can be realized because the required coil current converges to infinite for certain angular rotor positions. One coil current converging to infinite for the bearing forces is sufficient to disqualify the topology as a bearingless motor. The $\mathbf{T}_m$ matrix of the remaining case with $p = 3$ is plotted in Fig. 4. For the sake of visibility, exemplary values have been used for the force–current and torque–current factors to draw the matrices in the following ($k_{I,\text{Fr}} = 1$, $k_{I,\text{Ft}} = 0.7$, and $k_{I,\text{Tn}} = 0.5$). It basically shows the resulting force or torque in dependence on the rotor angle if a constant current is applied to one of the coils (labeled in Fig. 4). The corresponding $\mathbf{K}_m$ matrix is shown in Fig. 5. It shows which current has to be applied to the stator coils (labeled in the figure) in order to create a constant force or a constant torque. The bearing currents in Fig. 5 are finite over the whole angular range. This is a mandatory prerequisite for levitation, which can be stabilized with an adequate control implementation (e.g., PID; see Fig. 17), provided that the power electronic converter can supply the required control currents with sufficient bandwidth.

However, for the torque generation, the current in Fig. 5 converts to infinite for two specific angular rotor positions, in

which case the producible torque becomes zero. The third row entries of the matrix in this case are calculated as

$$\mathbf{K}_m(3, n) = \frac{1}{3 \cdot k_{I,\mathrm{Tn}} \cdot \sin(\varphi_{\mathrm{elec}})}. \tag{19}$$

If, for a certain topology, the bearing has been proved possible but the torque function requires infinite current for certain rotor angles, alternative torque current functions can be applied. The most logic adaption would be to stick to the curve plotted in the third plot of Fig. 5 and to limit it when the required current becomes too large. As a consequence, nonconstant torque will result, and it will still lower to zero for the specific rotor angles. Since it is anyways not possible to create a constant torque, alternative current functions can be considered as well. A meaningful torque current would follow the function

$$\frac{\sin(\varphi_{\mathrm{elec}})}{3k_{I,\mathrm{Tn}}}. \tag{20}$$

In this case, high current is applied whenever high torque can be generated (curve is close to zero in the original plot in Fig. 5), whereas the sinusoidal current from (20) reaches zero for the same angular position for which no torque can be generated. With this alternative current form, a larger average current would result. However, the multiplication of the $\mathbf{T}_m$ matrix from Fig. 4 with the $\mathbf{K}_m$ matrix from Fig. 5 [with altered torque function as in (20)] would no longer yield the unity matrix

$$\mathbf{T}_m \bullet \mathbf{K}_m = \begin{pmatrix} 1 & 0 & 0 \\ 0 & 1 & 0 \\ 0 & 0 & \sin^2(\varphi_{\mathrm{elec}}) \end{pmatrix}. \tag{21}$$

This means that the torque would vary over the whole angular range, following the function of the square of a sine. Thus, for certain angular rotor positions, the producible torque becomes zero, or in other words, the drive of the motor shows single-phase characteristics.

Given that the bearing currents are not of sinusoidal shape, the control implementation becomes more complex. Moreover, it is not possible to run the motor with a star connection because of the three equal drive currents that do not annihilate each other. This means that one full-bridge is required for each coil.

It is obvious that such a motor arrangement with equal pole pair number and slot number will additionally suffer from cogging torque. Therefore, this undesired property needs to be further analyzed, particularly under the consideration that there are angular rotor positions where no active motor torque can be generated.

The cogging torque is highly influenced by the design of the whole motor (e.g., stator tooth width), resulting in different cogging torque characteristics, as it is shown in Fig. 6, where the normalized cogging torque is shown for three different cases. For the designs considered (D1–D3), the tooth width has been varied. The tooth opening angle in relation to the angle of one magnet (60° in the case of this motor with pole pair number 3) was varied from 80% (D1) to 45% (D2) and 10% (D3). In all three cases, there is zero cogging torque for specific electrical angles of 0°, 90°, 180°, and 270°. The difference arises from the fact that these specific angular positions can be
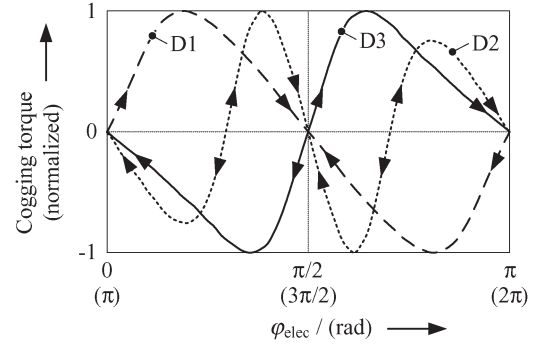

Fig. 6. Possible cogging torque (normalized) of a motor with three stator teeth and a pole pair number of three. Depending on certain design parameters, the cogging torque leads to stable angular rotor positions at either (solid line) 0°/180°, (dashed line) 90°/270°, or (dotted line) all four angles. The arrows indicate in which direction the rotor gets accelerated due to the cogging torque.

either stable or unstable. For the cogging torque shown with a solid line in Fig. 6, there are two stable angular positions for 0° and 180°. If the rotor is slightly rotated, a cogging torque arises which counteracts the movement. Hence, if there is no more external force acting onto the rotor, it would be brought back to this stable angular position due to the cogging torque. For the other two angular positions (90° and 270°) with zero cogging torque, the situation is different because a slight rotation leads to a cogging torque that accelerates the rotor further away until it reaches again a stable position at 0° or 180°. For an alternative design (dashed line), the situation is exactly the opposite because the stable angular positions are now for 90° and 270°. There is a third possibility (dotted line), where all four specific angles are stable angular positions. For this case, there are additional four angles with zero cogging torque, but for which the angular position is unstable.

Due to the single-phase characteristics of the drive, no torque can be generated for electrical angles of 0° and 180°. This situation is shown in Fig. 7, where the producible torque (normalized between zero and one) in dependence on the angular rotor position is shown for sinusoidal excitation. The motor can only work properly if the cogging torque leads to stable angular positions where the torque can be generated. For the torque characteristics at hand, this means that the cogging torque should be similar to the dashed line in Fig. 6. The cogging torque itself then stabilizes the rotor at angular positions where high torque can be produced in order to start the rotation. This situation is plotted in Fig. 7. Possibly, the motor can be feasible despite a cogging torque characteristic according to the dotted line in Fig. 6. However, if the cogging torque behaves according to the solid line, no feasible drive can be implemented. It can be concluded that this has to be considered during the design procedure in order to come up with a setup that works despite the single-phase characteristics of the drive.

B. Motors With Four Stator Teeth

From the four possible cases with $p = 1, 2, 3$, and 4, only rotors with an even pole pair number can be used for a bearingless motor. With a pole pair number of one or three, active control of the bearing would not be possible for certain angular
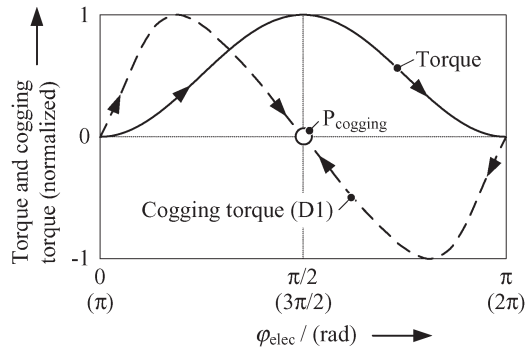
Fig. 7. Torque output (normalized between zero and one) is shown for (solid line) sinusoidal excitation according to (20) in dependence on the angular rotor position. The dashed line represents the cogging torque with design 1 from Fig. 6. In this case, the motor can accelerate because the stable positions due to the cogging torque (P_{cogging}) match with the positions where maximum torque can be produced.
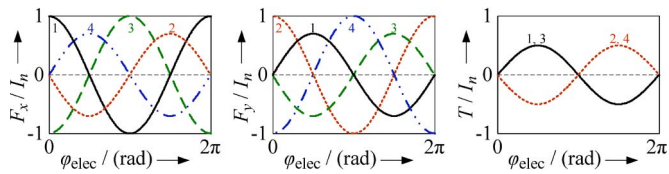

Fig. 8. $\mathbf{T}_m$ matrix of a bearingless motor with four stator teeth and a rotor with pole pair number 2.
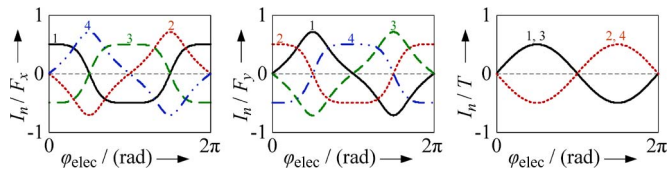

Fig. 9. $\mathbf{K}_m$ matrix of a bearingless motor with four stator teeth and a rotor with pole pair number 2. As the calculated torque currents would converge to infinite (as was the case for a three-slot motor), they have been replaced with a sinusoidal excitation.

rotor positions. For the other two cases with $p = 2$ and 4, the control is possible as will be shown further down. For the drive, however, no constant torque can be generated as was the case for the motor with three stator teeth.

A graphical representation of the $\mathbf{T}_m$ matrix for the case with pole pair number 2 is shown in Fig. 8, whereas its $\mathbf{K}_m$ matrix is shown in Fig. 9. The bearing can be controlled over the whole angular range, but for the torque generation, single-phase characteristic has to be accepted. Therefore, the currents in the third plot of the $\mathbf{K}_m$ matrix in Fig. 9 have already been replaced with a sine function. This leads to a torque with single-phase characteristic that varies with the square of a sine function as was the case for a motor with three stator teeth.

For the control, the nonsinusoidal bearing currents (representing a two-phase system) and the sinusoidal drive currents can be superimposed for each coil individually. The control could then be implemented with one full-bridge per coil. Since the sum of all currents over all coils is zero at any point, the four coils could be connected in star, and the power electronics could be reduced to four half-bridges [20], [21].
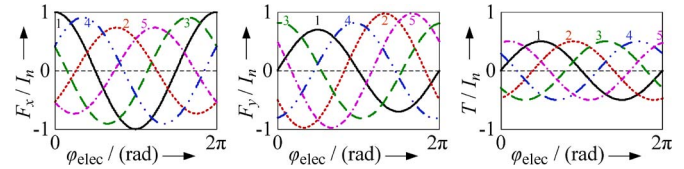

Fig. 10. $\mathbf{T}_m$ matrix of a bearingless motor with five stator teeth and a rotor with pole pair number 4.
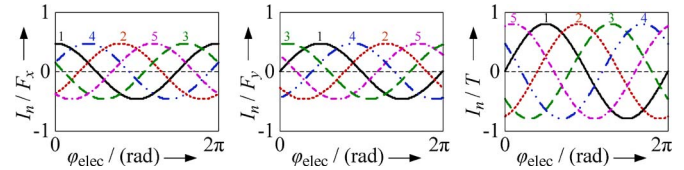

Fig. 11. $\mathbf{K}_m$ matrix of a bearingless motor with five stator teeth and a rotor with pole pair number 4.

For both possible rotor pole pair numbers with $p = 2$ and 4, the motor will suffer from cogging torque. Therefore, a similar analysis as for a motor with three stator teeth has to be undertaken in order to guarantee that the motor can start from the stable angular position imposed by the cogging torque.

C. Motors With Five Stator Teeth

A feasible topology for a five-slot motor with pole pair number 4 has already been shown at the beginning in Fig. 2. Graphical representations of the $\mathbf{T}_m$ and the $\mathbf{K}_m$ matrices for this topology are shown in Figs. 10 and 11, respectively. The $\mathbf{K}_m$ matrix reveals that sinusoidal currents can be applied for both bearing force and torque generation. Therefore, constant torque and bearing forces can be generated independent of the angular rotor position. Moreover, a star connection of all five coils is possible, and the motor could run with one single five-phase inverter.

In a similar way, the topology with pole pair number 2 can be implemented but only with sinusoidal bearing currents, whereas the drive currents become distorted. For the cases with pole pair numbers 1 and 3, all the currents are strongly distorted. Moreover, if the radial and tangential force–current factors approach identical values, the control becomes impossible. For the case of pole pair number 5, single-phase characteristic would occur, as was the case previously for the topologies with three and four stator teeth. Given that there are alternative implementations for this motor, the topology with five stator teeth and ten rotor magnets is not recommendable.

The topologies with a pole pair number different from five do not suffer from cogging torque. However, there is another undesired property, namely, unbalanced magnetic pull in the center position. This means that, even if the rotor is perfectly centered in relation to the stator and no current is applied, there will be a resulting force that pulls the rotor into a certain direction. For a practical implementation, this force would have to be compensated by the bearing, leading to large bearing currents which do not really contribute to the motor performance itself. In the design of such a motor, one of the aims has to be to keep this unbalanced magnetic pull at a
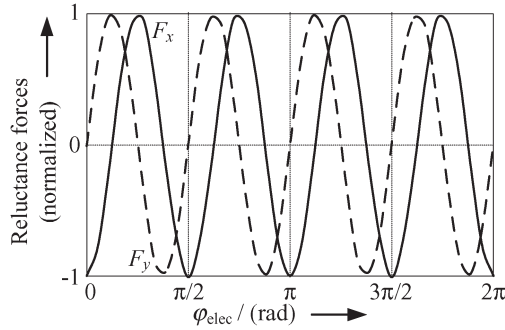
Fig. 12. Reluctance forces (normalized) acting on a centered rotor with eight rotor magnets in combination with a five-slot stator.

low value. In Fig. 12, the resulting forces into the x- and y-directions are shown in dependence on the electrical angle for the topology with pole pair number 4. It can be seen that, during a revolution of one pole pair, the force rotates four times around the rotor. Hence, during a complete revolution of the rotor, the unbalanced magnetic pull rotates 16 times. This apparently leads to higher dynamic requirements for the bearing control.

D. Motors With Six Stator Teeth

A motor consisting of a stator with six stator teeth allows for interesting topologies as well. It would be desirable to realize both bearing and drive using symmetric three-phase systems. For a rotor with pole pair number 2 or 5, this can be achieved as will be shown in the following for the first case. In Fig. 13, the $\mathbf{T}_m$ matrix for such a motor with pole pair number 2 is shown. The contributions of the tangential force and the radial force are shown separately. The corresponding $\mathbf{K}_m$ matrix can be realized with a sinusoidal six-phase system, as is shown in Fig. 14. In fact, always three nonadjacent coils can be connected in star and to one three-phase inverter, which allows for an easy implementation of the control. Moreover, the $\mathbf{K}_m$ matrix reveals that constant torque and bearing forces can be generated over the whole working range. As additional benefits, this motor only suffers from a very small cogging torque, and there is no unbalanced magnetic pull.

Alternative implementations with pole pair numbers 1 and 4 are not recommendable because they become uncontrollable if the radial and tangential force–current factors have similar values. For setups with pole pair numbers 3 and 6, the motors would suffer from a strong cogging torque; wherefore, this choice is also not favorable.

E. Comparison of Presented Motor Topologies

The motor characteristics derived previously are summarized in Table I for the most promising candidate of each stator variant. As stated before in (17), the pole pair number can also be chosen higher than the slot number, which can be beneficial because a thinner back iron ring is sufficient to avoid heavy saturation. Therefore, the next higher possible pole pair number showing the very same characteristics is given too. The motor setups with a five-slot and six-slot stator can generate constant torque with zero (or very small) cogging torque. Moreover,
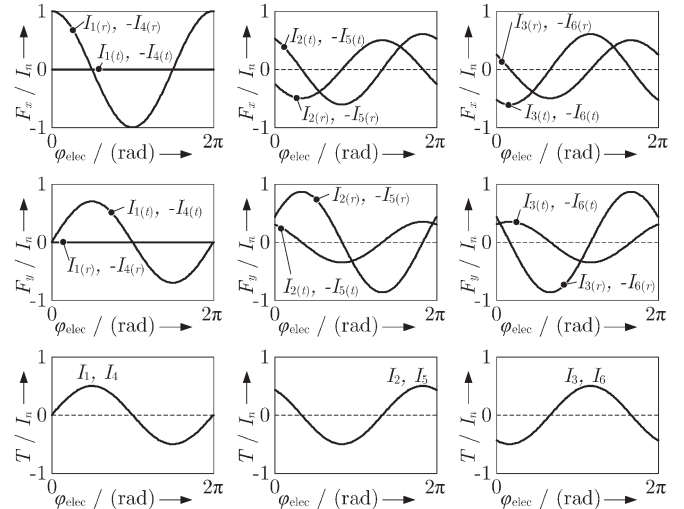

Fig. 13. $\mathbf{T}_m$ matrix of a bearingless motor with six stator teeth and a rotor with pole pair number 2. For the bearing forces, the separation into tangential (t) and radial (r) forces is shown.
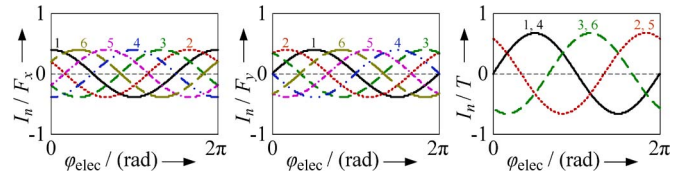

Fig. 14. $\mathbf{K}_m$ matrix of a bearingless motor with six stator teeth and a rotor with pole pair number 2.

TABLE I
MOTOR CHARACTERISTICS FOR DIFFERENT TOPOLOGIES

Slot number	3	4	5	6
Pole pair number	3, 6	2, 6	4, 9	2, 8
Constant torque	−	−	+	+
Zero cogging torque	−	−	+	+
No unbalanced magnetic pull	+	+	−	+
Sinusoidal control currents	−	−	+	+
Star-connection	−	+	+	+
Large winding space	+	+	−	−
Symmetric stator	−	+	−	+
Rank	4	2	2	**1**

sinusoidal control currents can be applied, and a star connection of the coils is possible (the latter is also possible for a four-slot topology). The large drawback of the five-slot topology is the unbalanced magnetic pull in the center position, which heavily lowers the efficiency of such a bearingless motor.

The advantage of the three-slot and the four-slot topologies is actually the small tooth number, which allows for large winding space resulting in a large possible magnetomotive force. For the passive bearing forces, a symmetric stator can be advantageous because the radial and tilting stiffness become less angular dependent.

Considering all the listed performance criteria, a motor setup with six stator teeth and a pole pair number of eight was found to be the best choice from the investigated topologies.

Therefore, a detailed design analysis of this setup is presented in the next section.

IV. DESIGN ANALYSIS FOR OPTIMAL TOPOLOGY

It was found that a topology with six stator teeth shows promising performance characteristics. Therefore, such a six-slot setup in combination with a 16-pole rotor has been optimized based on an extensive 3-D FE analysis. The choice for a rotor with a higher pole pair number was made because of practical considerations in terms of rotor manufacturing. The previously derived performance characteristics and the control are identical for such a rotor with pole pair number 8 as for one with pole pair number 2, as is stated in (17). Moreover, the torque output is similar for both rotor alternatives in case of equal coil excitation. For the targeted high-torque low-speed applications, the copper losses are clearly dominant compared to the iron losses. Hence, the disadvantage of increased iron losses, which obviously affects the rotor with higher pole number, can be neglected.

The optimization is carried out for a motor which can be run in a reactor of 500 L. For this case, an outer rotor diameter of 150 mm was identified to be ideal in terms of mixing behavior. Moreover, a magnetic gap between stator and rotor of 5 mm is required, which results in a fluid gap of about 2 mm in the final application if both stator and rotor encapsulation and the tank wall thickness are subtracted.

The stator has been optimized using bar-shaped stator teeth, which is recommendable for the bearing performance [22], [23]. In Fig. 15, the design optimization for the magnet thickness and the stator tooth width is shown in terms of torque and active and passive bearing force generation. Fig. 15(a) shows that higher torque can be achieved with thinner magnets and stator teeth because this would allow for higher magnetomotive force as a result of more available copper area, respecting maximum current densities of 3.5 (lower lines) and 14 (upper lines) A/mm^2, respectively. These current density values have been identified based on thermal constraints in case of simple air convection or if additional water cooling of the coils is employed. Fig. 15(b) shows the behavior of the radial bearing. The rotor has been radially displaced for 1 mm into the positive direction, resulting in a positive force. Therefore, a negative bearing force has to be generated actively (with a current density limited to 3.5 A/mm^2) to counteract the rotor movement. The solid lines show the sum of these two forces. The bearing is stable, if the resulting force is negative; otherwise, higher currents would be required. Additionally, Fig. 15(b) shows the behavior of the passive axial bearing (dashed lines). In this case, thicker magnets and thicker stator teeth are favorable because they increase the negative stiffness. Hence, a design compromise has to be made.

For the axial motor length, there is also a tradeoff between bearing stability and torque output. The slice motor concept is based on a low axial height. On the other hand, an increase in motor height would be beneficial for the torque. A motor height of 45 mm was found to be the optimal tradeoff. Table II summarizes all these optimal design values and the performance values for this design. The rated torque is 10 N · m, and the
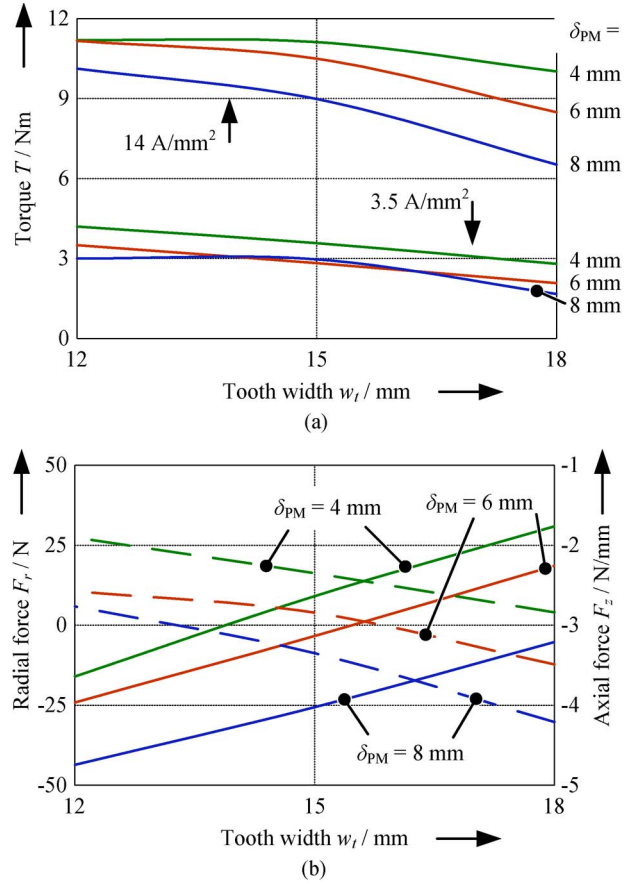

Fig. 15. Design optimization of the motor for (a) torque generation and (b) the bearing forces. The torque is shown in dependence on the magnet thickness ($\delta_{PM} = 4$, 6, and 8 mm) and the stator tooth width ($w_t = 12$, 15, and 18 mm) for two different excitation levels with maximum allowed current densities of 3.5 and 14 A/mm^2, respectively. (Solid line) For the bearing forces in (b), the sum of a positive displacement force (rotor of 1 mm displaced into the positive direction) and a negative active force (with a 3.5-A/mm^2 limit) is plotted. If this sum is negative, the bearing is stable for the chosen current limit; otherwise, higher currents would be required.

TABLE II
OPTIMAL DESIGN AND PERFORMANCE VALUES

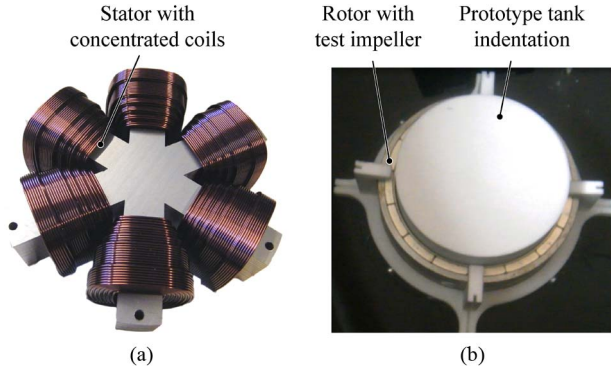| Parameter	Symbol	Value
Stator slot number	q	6
Pole pair number	p	8
Outer rotor diameter	d_R	148 mm
Magnetic gap thickness	δ_m	5 mm
Stator diameter	d_S	116 mm
Magnet thickness	δ_{PM}	6 mm
Back iron thickness	δ_{BI}	5 mm
Stator tooth width	w_t	15 mm
Machine length	l	45 mm
Winding number	N_{coil}	300
Tangential force-current factor	$k_{I,Ft}$	4.3 N/A
Radial force-current factor	$k_{I,Fr}$	5.9 N/A
Torque-current factor	$k_{I,Tn}$	0.34 Nm/A
Radial stiffness	k_r	-38.77 N/mm
Axial stiffness	k_z	3.2 N/mm
Tilting stiffness	k_ς	133 mNm/°
Rated torque	T	10 Nm
Rated angular speed	ω	50 s^{-1}
Rated power	P_{Mot}	500 W

(a)

(b)

Fig. 16. (a) Stator with six concentrated coils is buried below a cup, which represents (b) the tank indentation. A test impeller is mounted onto the rotor, which is then levitated inside the tank.
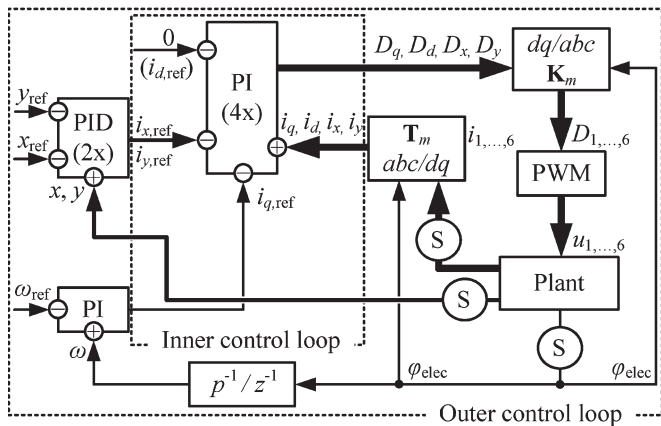

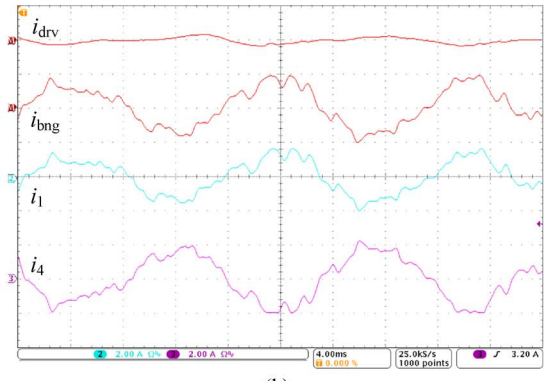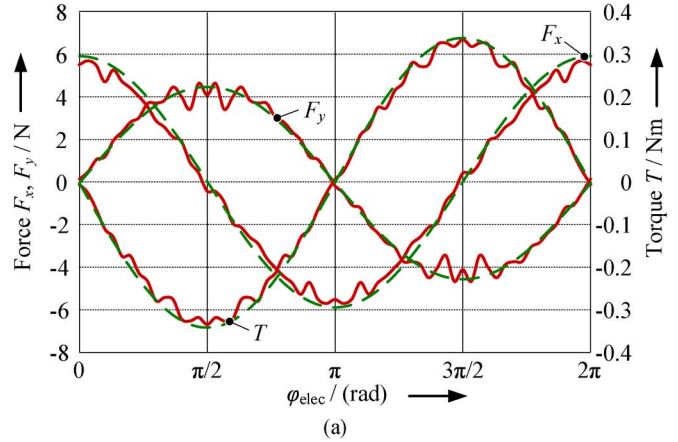Fig. 17. Control scheme for the bearingless mixer.

(a)

(b)

Fig. 18. Comparison of the theoretical values derived in Section III with (a) 3-D FE simulations and (b) measurements during rotation at 500 r/min with the reference position displaced from the center. (Current scales: 2 A/div; time scale: 4 ms/div).

rated angular speed is 50 s^{-1}, which results in a rated motor power of 500 W.

V. VERIFICATION WITH PROTOTYPE

A prototype setup has been realized in order to confirm the simulation results and to test the motor in a practical manner. The stator is made of laminated steel (M400-50A), and one concentrated coil is mounted on each stator tooth, as is shown in Fig. 16(a). Together with the sensor system (for radial and angular position measurements), the stator is then placed below a cylindrical cup [see Fig. 16(b)]. This cup represents the tank indentation, which was mounted into a small tank in order to test a real application situation. The rotor ring (back iron and permanent magnets) with a simple test impeller attached to it levitates around the buried motor. The power electronics converter consists of two times three half-bridges connected to a dc-link capacitor [24].

Fig. 17 shows an overview of the implemented control. Both the radial and the angular positions are measured, and the latter is also used to calculate the rotor speed. The position and the speed are controlled in an outer control loop using proportional–integral–derivative (PID) and proportional–integral (PI) controllers, respectively. The outer control loop determines the required bearing and drive currents, which are controlled with PI controllers in an inner loop. Therefore, the

coil currents have to be measured too. Moreover, transformations are required between the three-phase system of the plant and a rotor-fixed coordinate system (field-oriented control). The information of the $\mathbf{T}_m$ and $\mathbf{K}_m$ matrices has to be integrated into these transformations too [19].

A comparison is shown in Fig. 18 for the sinusoidal waveforms which have been theoretically derived in Section III. In Fig. 18(a), the force and torque values resulting from the 3-D FE simulations are plotted (solid lines) and compared to the theoretically assumed sinusoidal values (dashed lines). A pretty good accordance can be seen. Additionally, the current of two opposite coils has been measured in Fig. 18(b) during a rotation with 500 r/min. From these two coil currents, the drive and bearing currents can be determined using addition or subtraction, respectively. The reference value for the position (see Fig. 17) has been displaced by 1 mm from the center. Therefore, a certain bearing current is permanently required, which rotates synchronously with the rotor. Sinusoidal shapes can be seen too with a certain amount of higher frequency noise.

An acceleration test in an experimental tank setup has been undertaken, and the corresponding measurements are shown in Fig. 19. In the beginning, the rotor (with mixing head) is levitated at standstill. Then, it is accelerated in three steps to 300 r/min. During the whole operation, the radial rotor position is very stable and deviates less than 5% from the center position in relation to the total fluid gap. The bearing currents are
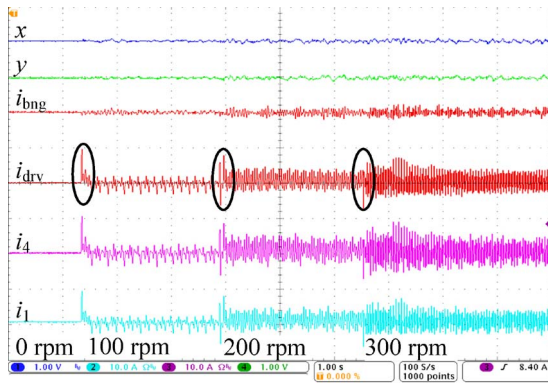
Fig. 19. Acceleration test in a test water tank. The measured position shows a very stable bearing performance, and only a small bearing current is required. The drive current increases with the speed, as the load increases. The acceleration peaks are circled. (Current scales: 10 A/div; position scales: 1 V/div (corresponds to 0.7 mm/div); time scale: 1 s/div).

only slightly elevated during the rotation because disturbances due to the mixed water have to be counteracted. The drive current depends on the load which is mixing the water. High currents are observed during the acceleration phases (marked with circles).

VI. CONCLUSION

Possible topologies for bearingless motors in exterior rotor construction have been compared in terms of performance characteristics and control effort. From the investigated setups with slot numbers of three to six in combination with varying rotor pole pair numbers, the best choice was found to be a six-slot/16-pole motor. Based on a 3-D FE analysis, the optimal design was derived and finally implemented in a prototype, which was successfully operated both in air and in a test water tank.

REFERENCES

[1] D. Mazzei, F. Vozzi, A. Cisternino, G. Vozzi, and A. Ahluwalia, "A high-throughput bioreactor system for simulating physiological environments," *IEEE Trans. Ind. Electron.*, vol. 55, no. 9, pp. 3273–3280, Sep. 2008.

[2] S. Ye and K. T. Chau, "Chaoization of DC motors for industrial mixing," *IEEE Trans. Ind. Electron.*, vol. 54, no. 4, pp. 2024–2032, Aug. 2007.

[3] S. S. Ozturk and W.-S. Hu, *Cell Culture Technology for Pharmaceutical and Cell-Based Therapies*. New York: Taylor & Francis, 2006.

[4] J. A. Asenjo and J. C. Merchuk, *Bioreactor System Design*. New York: Marcel Dekker, 1995.

[5] K. van't Riet and J. Tramper, *Basic Bioreactor Design*. New York: Marcel Dekker, 1991.

[6] M. A. Henson, "Biochemical reactor modeling and control," *IEEE Control Syst. Mag.*, vol. 26, no. 4, pp. 54–62, Aug. 2006.

[7] G. Catapano, P. Czermak, R. Eibl, D. Eibl, and R. Pörtner, "Bioreactor design and scale-up," in *Cell and Tissue Reaction Engineering: Principles and Practice*, vol. 1, 1st. ed. Berlin, Germany: Springer-Verlag, 2009, pp. 173–259.

[8] M. Ooshima and C. Takeuchi, "Magnetic suspension performance of a bearingless brushless DC motor for small liquid pumps," *IEEE Trans. Ind. Appl.*, vol. 47, no. 1, pp. 72–78, Jan./Feb. 2011.

[9] W. Gruber, W. Amrhein, and M. Haslmayr, "Bearingless segment motor with five stator elements—Design and optimization," *IEEE Trans. Ind. Appl.*, vol. 45, no. 4, pp. 1301–1308, Jul./Aug. 2009.

[10] H. Sugimoto, K. Kamiya, R. Nakamura, J. Asama, A. Chiba, and T. Fukao, "Design and basic characteristics of multi-consequent-pole bearingless motor with bi-tooth main poles," *IEEE Trans. Magn.*, vol. 45, no. 6, pp. 2791–2794, Jun. 2009.

[11] S. Zhang and F. L. Luo, "Direct control of radial displacement for bearingless permanent-magnet-type synchronous motors," *IEEE Trans. Ind. Electron.*, vol. 56, no. 2, pp. 542–552, Feb. 2009.

[12] T. Tera, Y. Yamauchi, A. Chiba, T. Fukao, and M. A. Rahman, "Performance of bearingless and sensorless induction motor drive based on mutual inductances and rotor displacements estimation," *IEEE Trans. Ind. Electron.*, vol. 53, no. 1, pp. 187–194, Feb. 2006.

[13] M. Ooshima, A. Chiba, T. Fukao, and M. A. Rahman, "Design and analysis of permanent magnet-type bearingless motors," *IEEE Trans. Ind. Electron.*, vol. 43, no. 2, pp. 292–299, Apr. 1996.

[14] Y. Christi and M. Moo-Young, "Clean-in-place systems for industrial bioreactors: Design, validation and operation," *J. Ind. Microbiol. Biotechnol.*, vol. 13, no. 4, pp. 201–207, Jul. 1994.

[15] R. Schoeb and N. Barletta, "Principle and application of a bearingless slice motor," *JSME Int. J.*, vol. 40, no. 4, pp. 593–598, Dec. 1997.

[16] S. Silber and W. Amrhein, "Bearingless single-phase motor with concentrated full pitch windings in exterior rotor design," in *Proc. 6th Int. Symp. Magn. Bearings*, 1996, pp. 476–485.

[17] T. Yamada, Y. Nakano, J. Asama, A. Chiba, T. Fukao, T. Hoshino, and A. Nakajima, "Outer rotor consequent-pole bearingless motor with improved start-up characteristics," *IEEE Trans. Magn.*, vol. 44, no. 11, pp. 4273–4276, Nov. 2006.

[18] T. Reichert, T. Nussbaumer, W. Gruber, and J. W. Kolar, "Bearingless permanent-magnet motor with 4/12 slot–pole ratio for bioreactor stirring applications," *IEEE/ASME Trans. Mechatronics*, vol. 16, no. 3, pp. 431–439, Jun. 2011.

[19] T. Reichert, T. Nussbaumer, and J. W. Kolar, "Bearingless 300-W PMSM for bioreactor mixing," *IEEE Trans. Ind. Electron.*, vol. 59, no. 3, pp. 1376–1388, Mar. 2012.

[20] K. Raggl, T. Nussbaumer, and J. W. Kolar, "Comparison of separated and combined winding concepts for bearingless centrifugal pumps," *J. Power Electron.*, vol. 9, no. 2, pp. 243–258, Mar. 2009.

[21] S. Silber, W. Amrhein, P. Bösch, R. Schoeb, and N. Barletta, "Design aspects of bearingless slice motors," *IEEE/ASME Trans. Mechatronics*, vol. 10, no. 6, pp. 611–617, Dec. 2005.

[22] P. Karutz, T. Nussbaumer, W. Gruber, and J. W. Kolar, "Acceleration-performance optimization for motors with large air gaps," *IEEE Trans. Ind. Electron.*, vol. 57, no. 1, pp. 52–60, Jan. 2010.

[23] P. Karutz, T. Nussbaumer, W. Gruber, and J. W. Kolar, "Saturation effects in high acceleration bearingless slice motors," in *Proc. IEEE Int. Symp. Ind. Electron.*, 2008, pp. 472–477.

[24] M. T. Bartholet, T. Nussbaumer, D. Krahenbühl, F. Zürcher, and J. W. Kolar, "Modulation concepts for the control of a two-phase bearingless slice motor utilizing three-phase power modules," *IEEE Trans. Ind. Appl.*, vol. 46, no. 2, pp. 831–840, Mar./Apr. 2010.

Thomas Reichert (S'09) was born in Schaffhausen, Switzerland, in 1983. He received the M.Sc. degree in electrical engineering and information technology from the Swiss Federal Institute of Technology (ETH) Zurich, Zurich, Switzerland, in 2008, where he is currently working toward the Ph.D. degree in the Power Electronic Systems Laboratory, working on high-torque magnetically levitated motors. The focus during his studies has been on mechatronics, robotics, power systems, and control. During his Master's thesis work, he simulated rotor dynamics and implemented a magnetic bearing for a megaspeed drive.

Thomas Nussbaumer (S'02–M'06) was born in Vienna, Austria, in 1975. He received the M.Sc. (with honors) degree in electrical engineering from Vienna University of Technology, Vienna, Austria, in 2001 and the Ph.D. degree from the Power Electronic Systems (PES) Laboratory, Swiss Federal Institute of Technology (ETH) Zurich, Zurich, Switzerland, in 2004.

From 2001 to 2006, he was with the PES, where he conducted research on modeling, design, and control of three-phase rectifiers, power factor correction techniques, and electromagnetic compatibility. Since 2006, he has been with Levitronix GmbH, Zurich, where he is currently working on bearingless motors, magnetic levitation, and permanent-magnet motor drives for semiconductor and biotechnology industry. His current research is focused on compact and high-performance mechatronic systems including novel power electronics topologies, control techniques, drive systems, sensor technologies, electromagnetic interference, and thermal aspects.

Johann W. Kolar (F'10) received the M.Sc. and Ph.D. (*summa cum laude/promotio sub auspiciis praesidentis rei publicae*) degrees from Vienna University of Technology, Vienna, Austria.

He initiated and/or is the Founder/Cofounder of four spin-off companies targeting ultrahigh speed drives, multidomain/level simulation, ultracompact/efficient converter systems, and pulsed-power/electronic energy processing. Since 1984, he has been an Independent International Consultant in close collaboration with Vienna University of Technology in the fields of power electronics, industrial electronics, and high-performance drives. He has proposed numerous novel converter topologies and modulation/control concepts, e.g., the Vienna rectifier, the Swiss rectifier, and the three-phase ac–ac sparse matrix converter. He has published over 450 scientific papers in international journals and conference proceedings and has filed more than 85 patents. Since February 1, 2001, he has been the Professor and Head of the Power Electronic Systems Laboratory, Swiss Federal Institute of Technology (ETH) Zurich, Zurich, Switzerland. The focus of his current research is on ac–ac and ac–dc converter topologies with low effects on the mains, e.g., for data centers, more electric aircraft, and distributed renewable energy systems, and on solid-state transformers for smart microgrid systems. Further main research areas are the realization of ultracompact and ultraefficient converter modules employing the latest power semiconductor technology (SiC and GaN), micropower electronics and/or power supplies on chip, multidomain/scale modeling/simulation and multiobjective optimization, physical model-based lifetime prediction, pulsed power, and ultrahigh-speed and bearingless motors.

Dr. Kolar is a member of the Institute of Electrical Engineers of Japan (IEEJ) and of international steering committees and technical program committees of numerous international conferences in the field (e.g., Director of the Power Quality Branch of the International Conference on Power Conversion and Intelligent Motion). He is the Founding Chairman of the IEEE Power Electronics Society (PELS) Austria and Switzerland Chapter and the Chairman of the Education Chapter of the European Power Electronics and Drives (EPE) Association. He served as an Associate Editor of the IEEE TRANSACTIONS ON INDUSTRIAL ELECTRONICS from 1997 to 2000, and he has been serving as an Associate Editor of the IEEE TRANSACTIONS ON POWER ELECTRONICS since 2001. Since 2002, he has also been an Associate Editor of the *Journal of Power Electronics* of the Korean Institute of Power Electronics and a Member of the Editorial Advisory Board of the *IEEJ Transactions on Electrical and Electronic Engineering*. He was the recipient of the Best Transactions Paper Award of the IEEE Industrial Electronics Society in 2005, the Best Paper Award of the International Conference on Power Electronics (ICPE) in 2007, the First Prize Paper Award of the IEEE Industry Applications Society (IAS) Industrial Power Converter Committee (IPCC) in 2008, the Annual Conference of the IEEE Industrial Electronics Society (IECON) Best Paper Award of the IEEE Industrial Electronics Society (IES) Power Electronics Technical Committee (PETC) in 2009, the IEEE PELS Transaction Prize Paper Award 2009, the Best Paper Award of the IEEE/ASME TRANSACTIONS ON MECHATRONICS 2010, the IEEE PELS Transactions Prize Paper Award 2010, the Best Paper First Prize Award at the Energy Conversion Congress & Exhibition (ECCE) Asia 2011, and the First Place IEEE IAS Society Prize Paper Award 2011. Furthermore, he was the recipient of the ETH Zurich Golden Owl Award 2011 for excellent teaching. He also was the recipient of an Erskine Fellowship from the University of Canterbury, Christchurch, New Zealand, in 2003. In 2006, the European Power Supplies Manufacturers Association named the Power Electronics Systems Laboratory, ETH Zurich, as the leading academic research institution in power electronics in Europe.